

# A Complete Brain Model (fix)

<sup>1</sup>Alexandra Warner, <sup>1</sup>Chris Johnson

<sup>1</sup>University of Utah, Salt Lake City UT; <sup>2</sup>Placeholder in case we need to put more refs

September 27, 2017

## Abstract

Here is some abstract text

## 1 Introduction

Introduction text.

## 2 Methods

### 2.1 Data Acquisition

To construct a high-resolution, personalized, anisotropic volume conductor whole-head model,  $T_1$ -,  $T_2$ - weighted, diffusion weighted, and functional MR scans were acquired on a healthy volunteer who is female and 23 years of age on a Skyra 3T full-body scanner (Siemens Medical Solutions). The  $T_1$ - weighted...

- Images were acquired using.... on a healthy volunteer (self, 24 years of age, female), MRI sequence (MPRAGE), – OSIRIX documentation

### 2.2 Preprocessing of Images

#### 2.2.1 MRI Correction

- T1 and T2 images were preprocessed using FSL for bias field correction

#### 2.2.2 DTI

- DWI was preprocessed using DTIPrep which corrects for movement, badly acquired images, etc.
- DWI was converted to DTI using Slicer - (module) after registration.

### 2.2.3 fMRI

- fMRI was preprocessed using the fcon\_1000 pipeline. (specific to the University of Utah), includes registration

### 2.2.4 Registration

All scans were registered to the  $T_1$  MRI. Since the subject did not move between the  $T_1$  and  $T_2$  MRIs, they did not need to be registered. However, the subject did move for the DWI. The cage (find proper name) was upgraded to the a higher resolution option. The subject did not move again for the fMRI.

To register the DWI to the  $T_1$  MRI, both scans must first be skull stripped which is to remove all tissues save for the brain. This was done using Brain Extraction Tool (BET2) in FMRIB Software Library (FSL). After the DWI was skull stripped, there was tissue remaining that was not part of the brain which was making the registration difficult. Both the  $T_1$  MRI and the DWI were manually fixed using Seg3D by generating thresholding masks and erasing non-brain tissue. The DWI was registered to the  $T_1$  MRI using 3D Slicer (ref) ([www.slicer.org](http://www.slicer.org)) with the skull stripped images with a rigid transform with six degrees of freedom. The 3D Slicer's linear registration transform output from registering the two brains was then applied to the full DWI image to register to the  $T_1$  MRI. The fMRI was registered as described in a later section using the f\_con1000 pipeline.

## FIGURES

Give each software a small definition?

## 2.3 MRI Segmentation of Tissues

Segmentation of the head tissues proved to be the most time consuming section of the pipeline. The head volume was segmented into air, cerebral spinal fluid (CSF), white matter, grey matter, skull, sinus, eyes, and scalp. Segmentation of the brain can be difficult due to the similar intensities of the different tissues, making merely applying a median filter and thresholding the image not enough. (show a figure of this happening?)

The brain was initially segmented by inputting a skull stripped  $T_1$  MRI into FSL FAST Segmentation. This outputs CSF, white matter, and grey matter layers as well as a bias-corrected  $T_1$  MRI. This method, compared with Freesurfer, Statistical Parametric Mapping through Matlab (SPM), Atlas Based Classification through 3D Slicer, and Seg3D methods alone, produced the best initial brain segmentation results for this data due to how well it filled in each tissue. (??) (three panel figure of FSL FAST results)

Although the FSL Fast results were a great improvement compared to the other segmentation trials, manual segmentation still needed to be done on those layers to add more detail and take out any cross over between the layers. Since white matter is the innermost layer, it was worked on first. All manual editing was done using Seg3D software. (ref) First a threshold layer was created from the FSL Fast output. Every slice in every direction was inspected and manually edited whether that was adding more detail that could be seen with the naked eye or cleaning up noise from FSL Fast. This manual editing of the white matter took roughly 40 hours of work. (Figure of before and after editing – hook detail!)

After the white matter was completed, a threshold layer for grey matter was created from the FSL Fast output. Each slice in every direction of the grey matter was inspected as well. The white

matter layer was removed from the grey matter using a boolean remove mask filter. Any holes between the two layers were decided manually. More detail was added to the grey matter folds to add to the CSF layer as well. The last part of editing the grey matter was decided to add a grey matter nucleus to the layer. The thresholding algorithms generated a lot of noise around these nuclei so they were segmented by hand, using the paintbrush tool, and added to the grey matter layer with a boolean or mask filter. The nuclei were also removed from the white matter layer using a boolean remove mask filter. The manual editing of the grey matter took roughly 20 hours of work. (figures of grey matter and nuclei)

After the grey and white matter layers were completed, the CSF layer was made by creating a solid threshold layer for the entire brain and removing the white and grey matter layers using a boolean remove mask filter. The white matter, grey matter, and CSF layers were then checked for holes, whether on the surface or the inside of the segmentation. Also a quality check on the layers was performed to ensure that the layers were at least two pixels wide. This is an important note for creating a hole-less tetrahedral mesh. The creation of the CSF layer and the manual editing and hole checking took roughly 4 hours of work. (??) (Figures of CSF? Figures of all three brain layers together?)

The skull and the sinus layers are the most difficult to segment using only an MRI because they both appear black in the image, and the volunteer did not have a CT scan. (define CT-scan) The first attempt to create a bone layer was first to use FSL's skull stripping using the BET2 tool to create a skull. Then to threshold the remainder of the bones in Seg3D from the  $T_1$  MRI and connect it to the skull from FSL. (figure and compare the two skull layers) Although this gave a decent skull for only having an MRI layer, the method to segment sinus layer was still to be determined. As a second method, the skull was estimated from an MR-based synthetic pseudo-CT. An improved iterative version of the patch-based method was used described by Torrado-Carvajal et al. [ref] that takes the  $T_1$  and  $T_2$  images as input, and synthesize the pseudo-CT based on both images providing more refined and accurate bone boundaries. MR input images were preprocessed to correct for MRI bias inhomogeneities (N4 bias correction tool in the Insight Toolkit)(ref?) prior to computing the pseudo-CT. (figure of the pseudo-CT output) This method gave a good starting place for skull segmentation, but still needed manual editing. After using a median filter (pixel radius?) and thresholding, each slice in each direction was manually edited by hand. (figure of segmentation) Since the volunteer has a permanent retainer in their mouth, the mouth was segmented as solid bone for now. This is not concerning because the EEG cap used did not cover the volunteer's mouth. (picture? explain EEG caps) The pseduo-CT image also provided a segmentation of the sinuses and esophagus by thresholding the black pixels. After the thresholding, the sinus layer was also manually edited. Quality checks were done on both layers to ensure that there were no holes and that the layers were at least two pixels thick. (figure) Manually editing the second skull and the sinuses took roughly 30-40 hours of work.

The eyes, skin, and air layers were simple, in comparison, to segment. The eyes were easily segmented by thresholding the  $T_2$  MRI. (figure of T2 axially) The skin layer was segmented by thresholding the entire volume and removing all of the previous layers using a boolean remove mask filter. A quality check was performed on the skin layer to ensure that it was at least two pixels thick. The important places to check for this is at the bridge of the nose and the bottom of the chin. (sagittal figure) Last, the air was segmented by thresholding the entire image and removing the solid skin layer. (how much time?) There was a check to ensure that the segmentation did not contain any holes between layers after they were removed. (should I explain this procedure?) To

create these three layers took roughly 8 hours of work, most of which was ensuring there were no holes in the segmentation. This is imperative to creating a quality mesh.

(Should I make a table instead for the amount of work?)

## 2.4 Finite Element Mesh Generation

- Tetrahedral mesh was generated using Cleaver.
- Due to the complexity of the segmentation, with a sizing field of 0.7, a mesh was generated with no holes but with 80M elements.
- To reduce the size of the mesh, a mesh was made with a sizing field of 1.0. The sizing field was then manipulated using SCIRun to change the scaling of the data (by 27?), and then input back into Cleaver and cleaved a new mesh. This mesh is 15.6M elements with no holes. This mesh contains one flat tetrahedra.
- Mesh simplification?

## 3 Conductivity Preparation

- Homogeneous conductivities
- White matter inhomogeneous tensor conductivities - scaling, ratios

### 3.1 Mathematical Modeling

### 3.2 Numerical Methods

### 3.3 Simulations

- Forward problem
- Include figures of SCIRun networks - how much detail??

END OF ALLY'S TEXT

#### 3.3.1 Experimental Methods

We induced episodes of acute, transient ischemia in anesthetized, open-chest swine ( $n = ??$ ) and canine ( $n = ??$ ) preparations. In each experiment, the heart was exposed and suspended in a pericardial cradle. A portion of the LAD was minimally dissected and fitted with a hydraulic occluder, which could be compressed to restrict coronary blood flow, thereby creating the transient ischemic condition, and then released to restore normal cardiac perfusion. Experimental protocols consisted of measuring extracellular potentials, both on the epicardial surface and within the myocardium, while applying stepwise increases of ischemic load.<sup>23</sup> To this end, two basic protocols were used to induce ischemia: 1) LAD blood flow was incrementally reduced by the occluder while maintaining a constant, often elevated, heart rate (supply ischemia) or 2) increases in the heart rate were applied while maintaining a constant, often restricted, LAD blood flow (demand ischemia). For purposes of this study, we do not consider the differences between supply and demand ischemia but rather

focus on the size, shape, and location of the zones within the heart that show an electrical response to the ischemic condition. All studies were performed in accordance with the Guide for the Care and Use of Laboratory Animals (NIH Pub. No 85-23, Revised 1996).

Customized sock and needle electrodes were used to acquire electrical recordings of both epicardial and intramural electrical potentials. A 247-electrode, flexible sock array,<sup>24</sup> with recording electrodes evenly distributed across the ventricles, acquired epicardial electrogram recordings. Twenty-five (25) flexible fiberglass plunge needles<sup>25</sup> were used to record intramural electrical activity. Plunge needles were constructed with 10 evenly spaced electrodes at 1.6 mm intervals along the shaft. Needles were placed in and around the perfusion bed of the occluded LAD. Sock and needle recordings were made periodically at a 1KHz sampling rate, the combination of which provided a *3-dimensional* electrical representation of the induced ischemic condition.

In addition to the acquisition of electrical recordings, digitized locations of sock electrodes and needle locations were extracted for postexperiment validation studies. After digitization, needle electrodes were removed and replaced with radio-opaque spacers prior to cardiac imaging in order to provide a registration reference.

Electrograms were calibrated, gain adjusted, and baseline corrected against control recordings, which had been taken immediately before each intervention. Poor quality electrograms, caused by broken lead connections or bad contacts, as well as electrograms without positive Q-wave deflections (identified as cavity electrodes) were discarded. The global root mean squared signal was computed from data recordings of both sock and needle electrodes. These signals were used to identify a point that lay at 40% of the distance between the J point and T wave peak (ST40%). Potential difference maps were generated at ST40%, which compared baseline recordings to those obtained during an ischemic episode. Potential differences, taken at ST40% during baseline conditions, were used to generate a threshold by which ischemic regions were identified as values exceeding two standard deviations. Sock recordings were used to validate simulation findings and will be addressed later. Needle electrodes were used to generate subject-specific ischemic zone geometries by identifying regions within a spatial neighborhood that met the above-mentioned ischemic thresholding criteria.<sup>26</sup>

### 3.4 Simulation Pipeline

A simulation pipeline was implemented in order to produce in silico models that were representative of experimental findings. Electrical data acquired during the experimental process, as well as imaging information acquired post experiment, were used to construct subject-specific, finite element, bioelectric simulations by way of the steps illustrated in Figure 1.

#### 3.4.1 Imaging and Segmentation

After completion of the experimental protocol, each heart was excised and scanned with a 7 tesla MRI scanner using FISP and FLASH MRI sequences. Diffusion tensor images (DTI) were also acquired to determine fiber direction. FISP scans rendered consistent, albeit low, contrast throughout the tissue - preserving edges near the field of view boundaries. FLASH scans, in comparison, provided images of high contrast within the center of the volume, which diminished steeply near the field of view boundaries. The advantages of both FISP and FLASH were combined in order to produce realistic, geometric segmentations of blood, cardiac tissue, and needles, using the Seg3D\*

---

\*<http://sci.utah.edu/software.html>

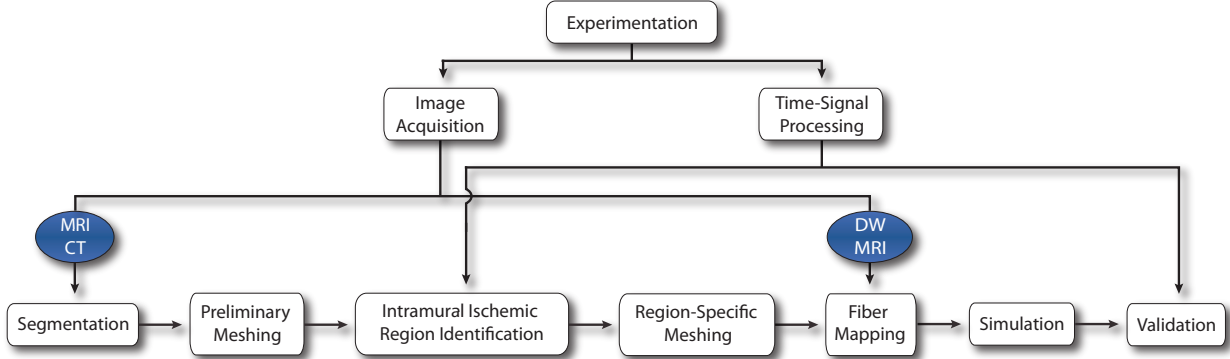


Figure 1: Ischemia Simulation Pipeline. Both image and time signals were extracted from experimental protocols of acute, induced ischemic preparations. Image data was used to generate geometries through segmentation and meshing. Intramural electrical data, recorded from plunge needles, were mapped to these meshes to define ischemic zone location. New meshes were generated with ischemic geometries imposed on which ischemic simulations were generated and validated against the original experimental data recorded from epicardial sock data.

open-source software package. Needle locations were readily identified within the scans as dark regions occupied by the radio-opaque spacers that were inserted at the end of the experimental phase. Diffusion-weighted MRI (DW-MRI) images were also obtained from which fiber orientation was derived.

### 3.4.2 Geometric Processing and Data Mapping

Segmentations were used to generate realistic *3-dimensional* geometries for use in subsequent finite element simulations (See Section 3.4.4). By using two open-source meshing packages, we were able to generate smooth, linear, subject-specific, boundary-conforming, tetrahedral meshes for use in simulations. First, segmentations were ported into the BioMesh3D\* software package to generate smoothed/tightened surface representations. BioMesh3D surface representations were used as input indicator functions to a second meshing package, Cleaver\*, from which the final mesh was derived. Cleaver is a multimaterial meshing package that produces structured meshes of tetrahedral elements with guaranteed minimum element angles,<sup>27</sup> resulting in quality meshes that require fewer computational resources. Cleaver, however, does not offer the surface-tightening features of BioMesh3D. As a result, meshes produced by Cleaver from standard MRI segmentations (with no surface tightening) would propagate the stair-stepped surfaces inherent in rasterized, volumetric data. By combining packages, we were able to produce smooth, structured meshes of guaranteed element quality.

Correspondence points derived from known sock and needle locations were used to register needle and sock electrode geometries within the cardiac mesh using the SCIRun problem-solving environment †. Processed data values were mapped to corresponding node locations within the cardiac mesh. Linear interpolation to local nodes was applied but restricted to the geometric convex hull of the needle locations. Extrapolation to outlying regions, not within the scope of needle locations, was not included.

To identify ischemic zones, potential difference maps were generated that removed baseline potentials from those observed during ischemic interventions. Difference map values within the specified needle region that exceeded a value greater than two standard deviations from baseline recordings were identified and labeled as ischemic. These new label masks were used to create a final mesh that contained three defined tissues (blood, healthy cardiac tissue, and ischemic cardiac tissue) that shared conforming surfaces - an important feature in static forward simulations when considering areas in proximity to potential sources.<sup>28</sup>

Finally, subject-specific fiber orientation was applied within the mesh. A vector field was defined by the principle eigenvector from DW-MRI images with all other cross-sectional fiber components regarded as isotropic. This vector field was normalized, aligned, and mapped to the cardiac mesh using weighted-average interpolation to provide a basis for anisotropic conductivity.

### 3.4.3 Mathematical Modeling

The cardiac mesh, with associated fiber structure and ischemic region, was used to solve the bidomain passive current flow equation:

$$\nabla \cdot (\bar{\sigma}_e + \bar{\sigma}_i) \nabla \phi_e = -\nabla \cdot \bar{\sigma}_i \nabla V_m \quad (1)$$

where  $\sigma_e$  and  $\sigma_i$  represent the extracellular and intracellular conductivity tensors, respectively.  $\phi_e$  is the extracellular potentials, and  $V_m$  represents the transmembrane potential.

In this model, it was assumed that the heart was surrounded by a perfect insulator, leading to a Neumann boundary condition on the epicardial surface. The endocardium, in contrast, allowed for extracellular, but not intracellular, current flow into the ventricular blood pool. Initial blood potentials were defined by Cauchy boundary conditions along the endocardial surface as shown in Equation 2.

$$\begin{cases} \nabla \cdot (\bar{\sigma}_e + \bar{\sigma}_i) \nabla \phi_e = -\nabla \cdot \bar{\sigma}_i V_m & x \in \Omega_H \\ \vec{n}_{epi} \cdot (\bar{\sigma}_e + \bar{\sigma}_i) \nabla \phi_e = 0 & x \in \partial\Omega_{H,epi} \\ \vec{n}_{endo} \cdot (\bar{\sigma}_e \nabla \phi_e) = -\vec{n}_b \cdot (\bar{\sigma}_b \nabla \phi_b) & x \in \partial\Omega_{H,endo} \\ \phi_e = \phi_b & x \in \partial\Omega_{H,endo} \\ \phi_i = 0 & x \in \Omega_b \end{cases} \quad (2)$$

where  $\Omega_H$  represents the cardiac volume;  $\partial\Omega_{H,epi}$  and  $\partial\Omega_{H,endo}$  the epicardial and endocardial surfaces, respectively;  $\phi_e$  and  $\phi_b$  correspond to potentials in the extracellular space and the blood, respectively.  $\vec{n}$  represents the normal, outward unit vector along the epicardial (*epi*), endocardial (*endo*), and blood (*b*) surfaces. The first equation specifies the relationship between transmembrane and extracellular potentials within the cardiac domain. The following four equations define the handling of currents and potentials along the cardiac surfaces. The blood, in all studies, was completely enclosed within the cardiac region and considered to have isotropic conductivity (See Figure 2 and Table 1).

Conductivity values within the tissue, as well as the blood pool, were normalized with respect to extracellular longitudinal values and matched those used in previous studies.<sup>10,29,30</sup> Table 1 shows the conductivity values used for this study. These conductivity values were chosen to be consistent with those previously defined by Johnston and Kilpatrick.<sup>31</sup> Conductivities within the ischemic region were reduced with respect to healthy values corresponding to the first 5 - 15 minutes after ischemic onset.

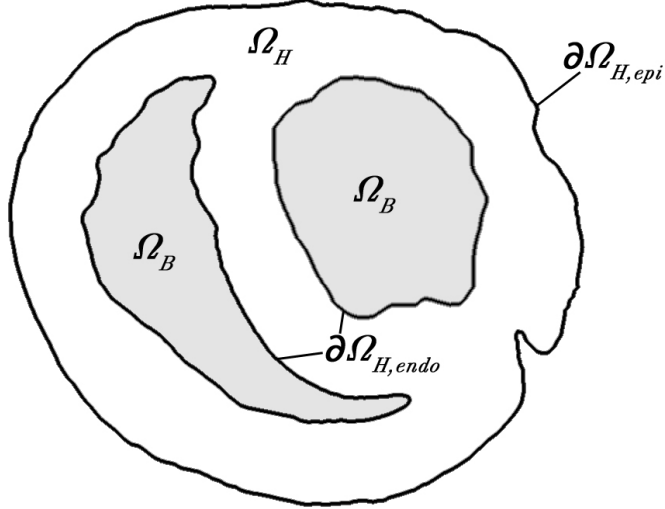


Figure 2: Bidomain equations are defined within the cardiac tissue  $\Omega_H$  and bounded by epicardial and endocardial boundaries  $\Omega_{H,epi}$  and  $\Omega_{H,endo}$ . Extracellular currents were allowed to flow into the blood volume  $\Omega_B$  along the endocardial boundary.

Table 1: Ratio applied to tensor conductivity values within healthy and ischemic regions.<sup>29</sup>

Conductivity Labels	Healthy Conductivity Values		Ischemic Conductivity Values	
	$\sigma_{el}$	1	$\sigma_{il}$	1/2
$\sigma_{et}$	1	1	1	1
$\sigma_{it}$	1/3	1/3	1/4	1/4
$\sigma_b$	1/20	1/20	1/20	1/20
	3	3	3	3

We defined a fixed transmembrane potential value ( $V_m$ ) of 30mV as the potential source for our forward simulations. The reduced transmembrane potential mimics the delayed activation of diseased tissue under ischemic conditions during the ST-segment. Healthy tissue was assigned a value of 0 mV, typical of the relatively quiescent state of healthy cardiac activation during the ST segment. Between healthy and ischemic tissue, a border zone was defined in which potentials progressed from the diseased to healthy states.

The border zone, the region between healthy and ischemic tissue, has been determined to be a necessary, and problematic, region to include in simulation studies.<sup>10,29,32</sup> In this study, we defined the border zone as a piecewise, continuous function represented by Equation 3 in which a Gaussian function defines the region from the ischemic zone boundary to a specified transition point,  $S_1$ . At  $S_1$  the border transitions to a linear, decreasing function that reduces to 0 (the value assigned to healthy tissue) at  $S_2$ . It is important to note that not all models, found in the literature, have applied border zones. For the sake of consistency and uniformity, however, we have imposed border regions into all of the forward simulations constructed in this paper. Table 2 shows the values

applied to Equation 3 for this study.

$$BZ = \begin{cases} V_m e^{\frac{-d^2}{2\sigma^2}} & d < S_1 \\ \Gamma - \frac{\Gamma}{S_2 - S_1}(d - S_1) & S_1 \leq d < S_2 \\ 0 & d \geq S_2 \end{cases} \quad (3)$$

where  $\Gamma = V_m e^{\frac{-(S_1)^2}{2\sigma^2}}$

Table 2: Values Used In Border Zone Determination.

Label	Definition	Value
$V_m$	Transmembrane Potential	30 mV
$\sigma$	Gaussian RMS Width	5 mm
$S_1$	First Transition Distance	8 mm
$S_2$	Second Transition Distance	11 mm
$d$	<i>distance</i>	<i>variable</i>

### 3.4.4 Numerical Methods

Solutions to Equation 1 were computed using finite element methods. By applying Green's divergence theorem to Equation 1, the following weak formulation is generated

$$\int ((\bar{\sigma}_e + \bar{\sigma}_i) \nabla \phi_e) \cdot \nabla \psi(\bar{x}) d\bar{x} = - \int (\bar{\sigma}_i \nabla V_m) \cdot \nabla \psi(\bar{x}) d\bar{x}, \quad \forall \psi \in \Omega \quad (4)$$

where,  $\Omega$  (see Section Section 3.4.2) is the linear, finite element mesh,  $\psi$  represents the finite element basis functions characterized by local hat functions associated with mesh nodes. By applying this formulation to the finite dimensional mesh, we can reduce Equation 4 to a system of linear equations

$$A\phi_e = -RV_m \quad (5)$$

where  $A$  and  $R$  represent stiffness matrices defined by  $A_{j,k} = \langle \nabla \psi_j, (\bar{\sigma}_e + \bar{\sigma}_i) \nabla \psi_k \rangle_\Omega$  and  $R_{j,k} = \langle \nabla \psi_j, \bar{\sigma}_i \nabla V_m \rangle_\Omega$ , while  $\phi_e$  and  $V_m$  represent extracellular and transmembrane potentials, respectively.<sup>33</sup>

We used the open-source, SCIRun problem solving environment<sup>34</sup> to apply parameters and to solve Equation 5 numerically. Within the SCIRun environment, fiber orientation and conductivity tensors were applied to the mesh, initial and boundary conditions were defined, and border regions were generated in order to compute extracellular potentials by way of a conjugate gradient method with a Jacobi preconditioner.

### 3.4.5 Comparison Approaches

Epicardial potentials compared using CC, RMS Error, and DICE correlation...Do it first, then explain it.

### **3.4.6 Validation**

In order to validate solutions of the ischemic condition, experimental data was compared to simulated solutions. Experimental data were mapped to the mesh by digitizing and later registering sock electrodes to points identified on the surface of the cardiac mesh. Potential data from sock electrodes were interpolated onto the ventricular surfaces and compared to simulated potentials on a node-to-node correspondence. RMS error and the correlation coefficient between simulated epicardial potentials and experimental sock data were generated to assess accuracy of simulation results.

## **4 Results**

## **5 Discussion**

Write Me

## **6 Conclusion**

Write Me

## **7 Acknowledgements**

Support for this research comes from the the NIH NCRR Center for Integrative Biomedical Computing ([www.sci.utah.edu/cibc](http://www.sci.utah.edu/cibc)), NIH NCRR Grant No. 5P41-RR012553-08, the Nora Eccles Treadwell Foundation, and the Richard A. and Nora Eccles Harrison Fund for Cardiovascular Research.

## References

- [1] D. Hearse. Myocardial ischaemia: Can we agree on a definition for the 21<sup>st</sup> century? *Cardiovascular Research*, 28:1737–1744, 1994.
- [2] R P Holland and H Brooks. Precordial and epicardial surface potentials during myocardial ischemia in the pig. A theoretical and experimental analysis of the TQ and ST segments. *Circulation Research*, 37(4):471–480, 1975.
- [3] T H Lee, G W Rouan, M C Weisberg, D A Brand, E F Cook, D Acampora, and L Goldman. Sensitivity of routine clinical criteria for diagnosing myocardial infarction within 24 hours of hospitalization. *Ann. Intern. Med.*, 106(2):181–186, 1987.
- [4] R. Gianrossi, R. Detrano, D. Mulvihill, K. Lehmann, P. Dubach, A. Colombo, D. McArthur, and V. Froelicher. Exercise-induced ST depression in the diagnosis of coronary artery disease. A meta-analysis. *Circulation*, 80:87–98, 1989.
- [5] P.F. Salisbury, C.E. Cross, and P.A. Rieben. Acute ischemia of inner layers of the ventricular wall. *American Heart Journal*, 66:650–656, 1963.
- [6] T.W. Moir. Subendocardial distribution of coronary blood flow and the effect of antianginal drugs. *Circulation Research*, 30:621–627, 1972.
- [7] J.K. Kjekshus, P.R. Maroko, and B.E. Sobel. Distribution of myocardial injury and its relation to epicardial ST segment changes after coronary artery occlusion in the dog. *Cardiovascular Research*, 6:490–499, 1972.
- [8] K.A. Reimer, J.E. Lowe, M.M. Rasmussen, and R.B. Jennings. The wavefront phenomenon of ischemic cell death. Myocardial infarct size vs duration of coronary occlusion in dogs. *Circulation*, 56:786–794, 1977.
- [9] Bjrn Fredrik Nielsen, Xing Cai, Joakim Sundnes, and Aslak Tveito. Towards a computational method for imaging the extracellular potassium concentration during regional ischemia. *Mathematical Biosciences*, 220(2):118–130, 2009.
- [10] D J Swenson, J G Stinstra, B M Burton, K K Aras, L J Healy, and R S MacLeod. Evaluating the effects of border zone approximations with subject specific ischemia models. *World Congress on Medical Physics and Biomedical Engineering, September 7 - 12, 2009, Munich, Germany*, 25/4(Chapter 446):1680–1683, 2010.
- [11] Bruce Hopenfeld, Jeroen G Stinstra, and Rob S Macleod. The effect of conductivity on ST-segment epicardial potentials arising from subendocardial ischemia. *Ann Biomed Eng*, 33(6):751–763, 2005.
- [12] P R Johnston, D Kilpatrick, and C Y Li. The importance of anisotropy in modeling ST segment shift in subendocardial ischaemia. *IEEE Trans. Biomed. Eng.*, 48(12):1366–1376, 2001.
- [13] P Colli Franzone, L F Pavarino, and Simone Scacchi. Dynamical effects of myocardial ischemia in anisotropic cardiac models in three dimensions. *Mathematical Models and* , 17(12):1965–2008, 2007.

- [14] X Jie, V Gurev, and N Trayanova. Mechanisms of mechanically induced spontaneous arrhythmias in acute regional ischemia. *Circulation Research*, 106(1):185–92, 2010.
- [15] Mary C MacLachlan, Joakim Sundnes, Ola Skavhaug, Marius Lysaker, Bjrn Fredrik Nielsen, and Aslak Tveito. A linear system of partial differential equations modeling the resting potential of a heart with regional ischemia. *Mathematical Biosciences*, 210(1):238–252, 2007.
- [16] B Trénor, L Romero, JM Ferrero, J Sáiz, G Moltó, and JM Alonso. Vulnerability to reentry in a regionally ischemic tissue: a simulation study. *Ann Biomed Eng*, 35(10):1756–70, 2007.
- [17] M Wilhelms, O Dssel, and G Seemann. Simulating the impact of the transmural extent of acute ischemia on the electrocardiogram. *Computers In Cardiology. Proceedings*, pages 13–16, 2010.
- [18] D D Li, C Y CY Li, A C AC Yong, and D D Kilpatrick. Source of electrocardiographic ST changes in subendocardial ischemia. *Circulation Research*, 82(9):957–970, 1998.
- [19] Andrew J Pullan, Martin L Buist, Greg B Sands, Leo K Cheng, and Nicolas P Smith. Cardiac electrical activity-from heart to body surface and back again. *Journal of Electrocardiology*, 36:63–67, 2003.
- [20] R.B. Jennings, C.E. Ganote, and K.A. Reimer. Ischemic tissue injury. *American Journal of Pathology*, 81:179–198, 1975.
- [21] C. Steenbergen, C. Deleeuw, C. Barlow, B. Chance, and J.R. Williamson. Heterogeneity of the hypoxic state in perfused rat heart. *Circulation Research*, 41:606–615, 1977.
- [22] K.K. Aras. *Bioelectric Source Characterization Of Acute Myocardial Ischemia*. PhD thesis, The University of Utah, 2015.
- [23] K. Aras, B. Burton, D. Swenson, and R. MacLeod. Sensitivity of epicardial electrical markers to acute ischemia detection. *J Electrocardiol*, 47(6):836–841, 2014.
- [24] G. Arisi, E. Macchi, C. Corradi, R.L. Lux, and B. Taccardi. Epicardial excitation during ventricular pacing: Relative independence of breakthrough sites from excitation sequence in canine right ventricle. *Circ Res*, 71(4):840–849, 1992.
- [25] J.M. Rogers, S.B. Melnick, and J. Huang. Fiberglass needle electrodes for transmural cardiac mapping. *IEEE Trans Biomed Eng*, 49(12):1639–1641, 2002.
- [26] K.K. Aras, S. Shome, D.J. Swenson, J.G. Stinstra, and R.S. MacLeod. Electrocardiographic response of the heart to myocardial ischemia. In *Computers in Cardiology 2009*, pages 105–108, 2009.
- [27] J. Bronson, J.A. Levine, and R.T. Whitaker. Lattice cleaving: a multimaterial tetrahedral meshing algorithm with guarantees. *IEEE Transactions on Visualization and Computer Graphics (TVCG)*, pages 223–237, 2014.
- [28] D. Swenson, J.A. Levine, Z. Fu, J.D. Tate, and R.S. MacLeod. The effect of non-conformal finite element boundaries on electrical monodomain and bidomain simulations. *Computing in Cardiology*, (37):97–100, 2010.

- [29] B. Hopenfeld, J.G. Stinstra, and R.S. MacLeod. Mechanism for ST depression associated with contiguous subendocardial ischemia. *J Cardiovasc Electrophysiol*, 15(10):1200–1206, 2004.
- [30] J.G. Stinstra, B. Hopenfeld, and R.S. MacLeod. A model for the passive cardiac conductivity. *Int. J. Bioelectromag.*, 5(1):185–186, 2003.
- [31] P R Johnston. A cylindrical model for studying subendocardial ischaemia in the left ventricle. *Mathematical Biosciences*, 2003.
- [32] D Kilpatrick, P R Johnston, and D S Li. Mechanisms of ST change in partial thickness ischemia. *Journal of Electrocardiology*, 2003.
- [33] Dafang Wang, Robert M Kirby, Rob S Macleod, and Chris R Johnson. Inverse electrocardiographic source localization of ischemia: An optimization framework and finite element solution. *Journal of Computational Physics*, 250:403–424, 2013.
- [34] S G Parker and C R Johnson. SCIRun: A scientific programming environment for computational steering, 1995.